J|A|C|S
ARTICLES
Published on Web 03/25/2005

Studies of an Enneanuclear Manganese Single-Molecule Magnet

Stergios Piligkos,[†] Gopalan Rajaraman,[†] Monica Soler,[‡] Nadeschda Kirchner,[§] Joris van Slageren,[§] Roland Bircher,[¶] Simon Parsons,[#] Hans-Ulrich Güdel,[¶] Jens Kortus,[∥] Wolfgang Wernsdorfer,[⊥] George Christou,[‡] and Euan K. Brechin*[,†,#]

Contribution from the School of Chemistry, The University of Edinburgh, West Mains Road, Edinburgh, EH9 3JJ, U.K., Department of Chemistry, The University of Manchester, Oxford Road, Manchester, M13 9PL, U.K., Department of Chemistry, University of Florida, Gainesville, Florida 32611-7200, Laboratoire Louis Néel-CNRS, 38042 Grenoble, Cedex 9, France, Department of Chemistry and Biochemistry, The University of Bern, Freiestrasse 3, CH-3000, Berne 9, Switzerland, 1 Physikalisches Institut, Universitat Stuttgart, Pfaffenwaldring 57, 70550 Stuttgart, Germany, MPI für Festkörperforschung, Heisenbergstr. 1, D-70569 Stuttgart, Germany, and IPCMS - GMI, 23, rue du Loess, F-67034 Strasbourg, France

Received December 22, 2004; E-mail: ebrechin@staffmail.ed.ac.uk

Abstract: The reaction of $[Mn_3O(O_2CMe)_6(py)_3]$ with the tripodal ligand H_3thme (1,1,1-tris(hydroxymethyl)-ethane) affords the enneanuclear complex $[Mn_9O_7(O_2CCH_3)_{11}(thme)(py)_3(H_2O)_2]$ **1**·1MeCN·1Et$_2$O. The metallic skeleton of complex **1** comprises a series of 10 edge-sharing triangles that describes part of an idealized icosahedron. Variable temperature direct current (dc) magnetic susceptibility data collected in the 1.8−300 K temperature range and in fields up to 5.5 T were fitted to give a spin ground state of $S = {}^{17}/_2$ with an axial zero-field splitting parameter $D = -0.29$ cm^{-1}. Ac susceptibility studies indicate frequency-dependent out-of-phase signals below 4 K and an effective barrier for the relaxation of the magnetization of $U_{eff} = 27$ K. Magnetic measurements of single crystals of **1** at low temperature show time- and temperature-dependent hysteresis loops which contain steps at regular intervals of field. Inelastic neutron scattering (INS) studies on complex **1** confirm the $S = {}^{17}/_2$ ground state and analysis of the INS transitions within the zero-field split ground state leads to determination of the axial anisotropy, $D = -0.249$ cm^{-1}, and the crystal field parameter, $B_4^0 = 7(4) \times 10^{-6}$ cm^{-1}. Frequency domain magnetic resonance spectroscopy (FDMRS) determined the same parameters as $D = -0.247$ cm^{-1} and $B_4^0 = 4.6 \times 10^{-6}$ cm^{-1}. DFT calculations are fully consistent with the experimental findings of two Mn(II) and four Mn(III) ions "spin up" and three Mn(IV) ions "spin down" resulting in the $S = {}^{17}/_2$ spin ground state of the molecule, with $D = -0.23$ cm^{-1} and $U = 26.2$ K.

Introduction

Polymetallic clusters of paramagnetic transition metal ions can display the phenomenon of single-molecule magnetism (SMM) if they combine a relatively large spin ground state (S) with a large and negative (easy-axis-type) magnetoanisotropy (D).[1] This is a rare combination which results in a significant barrier to thermally activated magnetization relaxation, and thus far, is most often found in complexes containing manganese. Compared to other transition metals clusters of manganese are often characterized by large spin ground states, and this in conjunction with the presence of Jahn−Teller distorted Mn^{3+} ions makes manganese clusters ideal candidates for SMMs.[2] The most studied family of SMMs are the dodecanuclear complexes of formula $[Mn_{12}O_{12}(O_2CR)_{16}(H_2O)_x]^{n-}$ ($n = 0$, 1, 2; $x = 3$, 4), but manganese clusters ranging in nuclearity from 2−84 have displayed SMM behavior.[3] Because these molecules not only display magnetization hysteresis but also quantum tunneling of magnetization (QTM),[4] they are promising new

[#] The University of Edinburgh.
[†] The University of Manchester.
[‡] The University of Florida.
[⊥] Laboratoire Louis Néel.
[¶] University of Bern.
[§] University of Stuttgart.
[∥] MPI für Festkörperforschung.

(1) (a) Sessoli, R.; Gatteschi, D.; Hendrickson, D. N.; Christou, G. *MRS Bull.* **2000**, *25*, 66−71. (b) Sessoli, R.; Tsai, H.-L.; Schake, A. R.; Wang, S.; Vincent, J. B.; Folting, K.; Gatteschi, D.; Christou, G.; Hendrickson, D. N. *J. Am. Chem. Soc.* **1993**, *115*, 1804−1816. (c) Sessoli, R.; Gatteschi, D.; Caneschi, A.; Novak, M. A. *Nature* **1993**, *365*, 141−143. (d) Caneschi, A.; Gatteschi, D.; Sessoli, R.; Barra, A. L.; Brunel, L. C.; Guillot, M. *J. Am. Chem. Soc.* **1991**, 113, 5873−5874.

(2) Hendrickson, D. N.; Christou, G.; Ishimoto, H.; Yoo, J.; Brechin, E. K.; Yamaguchi, A.; Rumberger, E. M.; Aubin, S. M. J.; Sun, Z.; Aromi, G. *Mol. Cryst. Liq. Cryst.* **2002**, *376*, 301−313.

(3) See for example: (a) Tasiopoulos, A. J.; Vinslava, A.; Wernsdorfer, W.; Abboud, K. A.; Christou, G. *Angew. Chem., Int. Ed.* **2004**, *43*, 2117−2121. (b) Miyasaka, H.; Clérac, R.; Wernsdorfer, W.; Lecren, L.; Bonhomme, C.; Sugiura, K.; Yamashita, M. *Angew. Chem., Int. Ed.* **2004**, *43*, 2801−2805. (c) Murugesu, M.; Wernsdorfer, W.; Raftery, J.; Christou, G.; Brechin, E. K. *Inorg. Chem.* **2004**, *43*, 4203−4209. (d) Milios, C. J.; Raptopoulou, C. P.; Terzis, A.; Lloret, F.; Vicente, R.; Perlepes, S. P.; Escuer, A. *Angew. Chem., Int. Ed.* **2003**, *43*, 210−212. (e) Wittick. L. M.; Murray, K. S.; Moubaraki, B.; Batten, S. R.; Spiccia, L.; Berry, K. J. *Dalton Trans.* **2004**, 1003−1011.

(4) Friedman, J. R.; Sarachik, M. P.; Tejada, J.; Ziolo, R. *Phys. Rev. Lett.* **1996**, *76*, 3830−3833.

10.1021/ja042302x CCC: $30.25

Scheme 1. Tripodal Ligands H_3thme (left), H_3tmp, and H_4peol (right)

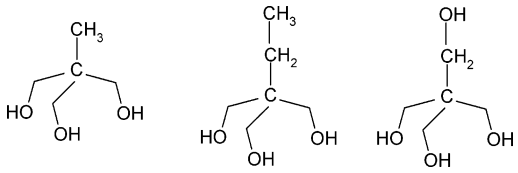

materials for data storage and quantum computing and, as such, are the focus of much attention.

To make clusters containing Mn^{3+} and/or Mn^{4+} ions, it is necessary to either oxidize simple Mn^{2+} salts in the presence of flexible organic bridging ligands, such as carboxylates, β-diketonates, and alkoxides, or to use the preformed metal triangles of formula $[Mn_3O(O_2CR)L_3]^{0/+}$. This last strategy has proved to be an extremely successful method.[5] The use of these triangles overcomes the lack of a suitable and simple Mn^{3+} precursor, although recently an SMM derived directly MnF_3 has been reported.[6] In an effort to produce large clusters with high spin ground states and possible SMM behavior, we have been exploring the reactivity of the tripodal ligand 1,1,1-tris-(hydroxymethyl)ethane and its analogues (Scheme 1) with oxo-centered manganese triangles. Previously these types of ligands have been used to great extent in the synthesis of oxomolybdenum and oxovanadium clusters, but it is only recently that their use has been extended to the synthesis of paramagnetic clusters of first-row transition metals.[7,8] We recently reported the syntheses, structures, and magnetic properties of a series of manganese rodlike complexes whose structures are based on a series of edge-sharing triangles and whose topology could be controlled by variation of carboxylate, tripod, and base.[9] We now report an extension to this methodology in the preparation and characterization of an enneanuclear manganese complex.

Experimental Section

Syntheses. All reactions were carried out in aerobic conditions using materials as received. The triangular species $[Mn_3O(O_2CCH_3)_6(py)_3]$ was made as previously described.

$[Mn_9O_7(O_2CCH_3)_{11}(thme)(py)_3(H_2O)_2]$ (1). $[Mn_3O(O_2CCH_3)_6(py)_3]$ (0.50 g, 1 equiv) and H_3thme (1 equiv) were stirred in MeCN (30 mL) for 12 h. The solution was then filtered and layered with Et_2O. Black crystals suitable for crystallography formed in 1 week. Anal. Calcd (found) for $Mn_9C_{42}H_{61}N_3O_{34}$: C, 30.64 (30.69); H, 3.73 (3.59); N, 2.55 (2.65); Mn, 30.03 (30.22).

X-ray Crystallography. Diffraction data were collected with Mo Kα X-radiation ($\lambda = 0.71073$ Å) on a Bruker Smart APEX diffractometer equipped with an Oxford Cryosystems low-temperature device operating at 150 K. An absorption correction was applied using the SADABS program;[10] the structure was solved using Patterson methods (DIRDIF)[11] and refined by full-matrix least squares against F^2 (Shelxtl)[10] using all unique data. H-atoms were treated either as part of a rotating rigid group or with a riding model. A cluster of peaks in the Fourier difference map in the region of the hexagon of oxygen atoms attached to Mn_{4-9} were interpreted as a 3-fold disordered set of two acetates and two coordinated water molecules. The acetates were restrained to be geometrically similar; the major component C-atoms were refined with anisotropic thermal parameters, the minor component only isotropically. Disordered solvent regions were treated in the manner described by van der Sluis and Spek.[11] This treated 276 e per cell or 69 e per formula unit. This fits quite well with 1MeCN and 1Et_2O (66 e) for formula unit. The values of $F(000)$, the density, μ, etc. reflect this assumption.

Other Measurements. Elemental analyses were performed by The University of Manchester Microanalytical Service.

Variable temperature magnetic susceptibility (dc and ac) measurements were made on a Quantum Design MPMS-XL SQUID magnetometer equipped with a 7 T magnet. Data were collected on powdered samples restrained in eicosane to prevent torquing. Diamagnetic corrections were applied using Pascal's constants. Magnetization versus field hysteresis and direct current (dc) decay measurements at temperatures below 1.8 K were performed on single crystals using an array of home-built micro-SQUIDs equipped with three orthogonal field coils, which allows the applied magnetic field to be turned in all directions.[12]

The INS experiments were performed on the inverted geometry time-of-flight spectrometer IRIS at the pulsed neutron spallation source ISIS at the Rutherford Appleton Laboratory, U.K., using the PG002 graphite analyzer with an analyzing energy of 1.84 meV. Data were collected at three temperatures (1.6, 12, and 20 K) and corrected for the background and detector efficiency by means of empty cell measurements and a vanadium reference. The time-of-flight to energy conversion and the data reduction were done using the GUIDE program. The instrumental resolution derived from a vanadium metal reference at the elastic position was 18 μeV. On IRIS, the ZnS detector banks cover the angular range $2\theta = 20-160°$, giving access to a momentum transfer range $Q = 0.3-1.8$ Å^{-1} at the elastic position. A 2.5 g fresh polycrystalline sample of undeuterated $[Mn_9O_7(OAc)_{11}(thme)(py)_3(H_2O)_2]$ was used. The sample was placed under helium in an aluminum hollow cylinder can with an outer diameter of 23 mm and a sample thickness of 2 mm. The container was inserted in a standard ILL orange cryostat.

FDMRS spectra were recorded on a polycrystalline powder pellet (mass = 179.16 mg, thickness = 0.1456 cm; diameter = 1 cm) using linearly polarized radiation in the frequency range of 2.8−5.0 cm^{-1} at temperatures of 1.8−30 K in the absence of an external magnetic field. The spectrometer has been described in the literature.[13,14]

The Naval Research Laboratory Molecular Orbital Library (NRLMOL) program package is an all-electron implementation of density-functional theory (DFT). NRLMOL combines large Gaussian orbital basis sets, numerically precise variational integration, and an analytical solution of Poisson's equation in order to accurately determine the self-consistent potentials, secular matrix, total energies, and Hellmann−Feynman−Pulay forces.[15] Starting from the X-ray structure we generated an isolated single molecule for the calculation. To reduce the computational cost we replaced the outer methyl groups with

(5) Sañudo, E. C. et al. *Polyhedron* **2003**, *22*, 2267−2271.
(6) Jones, L. F.; Rajaraman, G.; Brockman, J.; Murugesu, M.; Raftery, J.; Teat, S. J.; Wernsdorfer, W.; Christou, G.; Brechin, E. K.; Collison, D. *Chem.−Eur. J.* **2004**, *10*, 5180−5194.
(7) (a) Khan, M. I.; Zubieta, J. *Prog. Inorg. Chem.* **1995**, *43*, 1−149. (b) Cavaluzzo, M.; Chen, Q.; Zubieta, J. *J. Chem. Soc., Chem. Commun.* **1993**, 131−132. (c) Finn, R. C.; Zubieta, J. *J. Cluster Sci.* **2000**, *11*, 461−482.
(8) (a) Jones, L. F.; Batsanov, A.; Brechin, E. K.; Collison, D.; Helliwell, M.; Mallah, T.; McInnes, E. J. L.; Piligkos, S. *Angew. Chem., Int. Ed.* **2002**, *41*, 4318−4321. (b) Brechin, E. K.; Soler, M.; Christou, G.; Helliwell, M.; Teat, S. J.; Wernsdorfer, W. *Chem. Commun.* **2003**, 1276−1277. (c) Moragues-Cánovas, M.; Rivière, E.; Ricard, L.; Paulsen, C.; Wernsdorfer, W.; Brechin, E. K.; Mallah, T. *Adv. Mater.* **2004**, *13*, 1101−1105. (d) Shaw, R. et al. *Chem. Commun.* **2004**, 1418−1419.
(9) Rajaraman, G.; Murugesu, M.; Soler, M.; Wernsdorfer, W.; Helliwell, M.; Teat, S. J.; Christou, G.; Brechin, E. K. *J. Am. Chem. Soc.* **2004**, *126*, 15445−15457.
(10) Sheldrick, G. M. *SHELXTL*, version 5; Bruker AXS: Madison, Wisconsin, 1995.
(11) (a) van der Sluis, P.; Spek, A. L. *Acta Crystallogr., Sect. A* **1990**, *46*, 194−201. (b) Spek, A. L. *PLATON*, A Multipurpose Crystallographic Tool; Utrecht University: Utrecht, The Netherlands, 1998. (c) Incorporated into the *WinGX* suite: Farrugia, L. J. *J. Appl. Crystallogr.* **1999**, *32*, 837−838.
(12) Wernsdorfer, W. *Adv. Chem. Phys.* **2001**, *118*, 99−190.
(13) van Slageren, J. et al. *Phys. Chem. Chem. Phys.* **2003**, *5*, 3837−3843.
(14) Kozlov, G. V.; Volkov, A. A. In *Millimeter and Submillimeter Wave Spectroscopy of Solids*; Grüner, G., Ed.; Springer: Berlin, 1998.
(15) (a) Pederson, M. R.; Jackson, K. A. *Phys. Rev. B* **1990**, *41*, 7453−7461. (b) Jackson, K. A.; Pederson, M. R. *Phys. Rev. B* **1990**, *42*, 3276−3281. (c) Porezag, D. V.; Pederson, M. R. *Phys. Rev. A* **1999**, *60*, 2840−2847. (d) Pederson, M. R.; Porezag, D. V.; Kortus, J.; Patton, D. C. *Phys. Status Solidi B* **2000**, *217*, 197−218.

hydrogen leaving the magnetic core unchanged. This resulted in a cluster of 113 atoms used for the DFT calculation. The basis set for each Mn contained 11 s-like, 5 p-like, and 4 d-like contracted Gaussian orbitals with 20 exponents ranging from $0.04-3.6 \times 10^6$. The oxygen atoms were described by 8 s-, 4 p-, and 3 d-contracted orbitals using 13 bare Gaussians between 0.105 and 6.12×10^4. Nitrogen and carbon had the same number of contracted orbitals, with 13 bare Gaussians between 0.094 and 5.17×10^4 for N and 12 bare Gaussians between 0.077 and 2.22×10^4 for C. Finally, hydrogen had 5 s-like, 3 p-like, and 1 d-like orbitals with 6 exponents between 0.074 and 77.84. For all orbitals not corresponding to an atomic orbital we used the longest ranged single Gaussians. This basis set resulted in a total number of 3494 orbitals for the complete cluster. The calculations have been carried out using the generalized gradient approximation of Perdew, Burke, and Ernzerhof[16] to the exchange and correlation functional.

The magnetic anisotropy energy, which is the key property of any single-molecule magnet, arises mainly because of spin−orbit coupling and other relativistic terms in the Hamiltonian.[17] Pederson and Khanna have recently developed a method accounting for second-order contributions to the magnetic anisotropy energies.[18] This method relies on a simple albeit exact method for spin−orbit coupling and a second-order perturbative treatment of the spin Hamiltonian to determine the dependence of the total energy on spin projection and is implemented in the NRLMOL package. This method has been generalized to arbitrary symmetry and applied successfully to predict the magnetic anisotropy energies of several single-molecule magnets.[19]

Results and Discussion

Syntheses. Reaction of 1 equiv of H_3thme with the neutral triangle $[Mn_3O(O_2CMe)_6(py)_3]$ in MeCN leads to the formation of a dark brown/black solution and a light brown precipitate. Removal of the precipitate and subsequent layering of the brown/black solutions with Et_2O leads to the formation of crystalline $[Mn_9O_7(O_2CR)_{11}(thme)(py)_3(H_2O)_2]$ (**1**) after approximately 1 week. The yield is variable, but easily reproducible, varying from a minimum of approximately 15% to a maximum of 25%. As with many reactions involving manganese, there is likely to be many species in equilibrium in solution, with **1** being the least soluble. Indeed, the solution remains quite darkly colored after the crystallization of the products is complete. The fact that complex **1** is made from a mixed-valent triangle containing one Mn^{2+} ion and two Mn^{3+} ions and fully protonated tripodal ligands and is itself mixed-valent but containing two Mn^{2+}, four Mn^{3+}, and three Mn^{4+} ions means that its formation is a complicated mechanism involving deprotonation/protonation, structural rearrangements, and redox chemistry of many species present in solution.

It is interesting to note that the equivalent reactions to that which produces **1**, but using the triangles $[Mn_3O(O_2CR)_6(py)_3]$ where R = Ph or $C(CH_3)_3$ with the tripodal ligand H_3thme, afford the dodecanuclear and octanuclear manganese rodlike complexes $[Mn_{12}O_4(OH)_2(O_2CPh)_{12}(thme)_4(py)_2]$ **2** and $[Mn_8O_4(O_2C(CH_3)_3)_{10}(thme)_2(py)_2]$ **3**, respectively.[9] These compounds have metal topologies that are dominated by the presence of the tripodal ligands, not the carboxylates. The disposition of the three alkoxide arms of the trianion directs the formation of triangular M_3 units, where each arm of the ligand bridges one edge of the triangle. These triangular units then combine in an edge-sharing fashion to form complexes whose structures are based on rods. The length of the rod formed is dependent upon the identity of both the tripod and the carboxylates that occupy the vacant coordination sites. None of these rodlike complexes are formed from acetate containing manganese triangles, unless a separate capping ligand, such as triethanolamine, is added. This is most likely due to the solubility of the products containing acetate. Complexes **2** and **3** form quickly in reasonable yields directly from slowly evaporating solutions of MeCN. Complex **1** is not isolated as easily and does not appear from the same slow evaporation. It instead requires the diffusion of diethyl ether into the MeCN solutions and crystallization periods of up to 1 week.

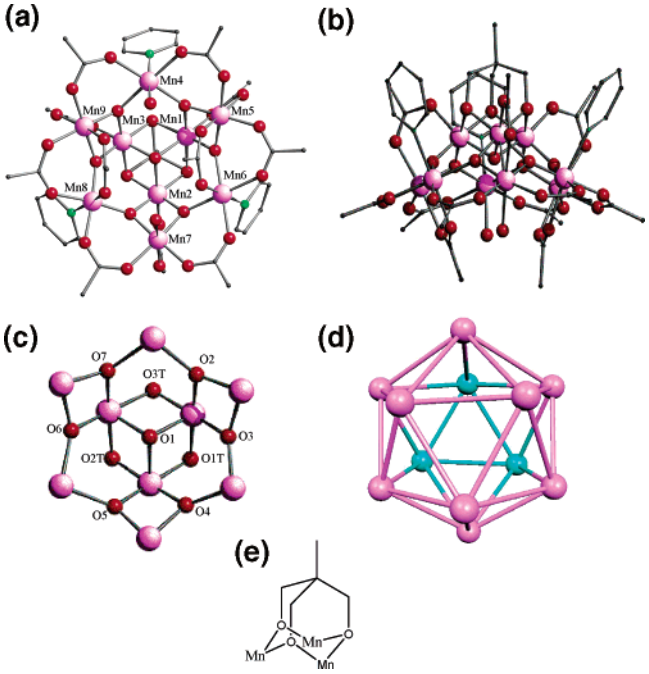

Figure 1. Structure of complex **1** in the crystal viewed from (a) above the central $[Mn^{III}_4Mn^{II}_2O_6]^{4+}$ ring; (b) perpendicular to the central $[Mn^{III}_4Mn^{II}_2O_6]^{4+}$ ring; (c) the metal−oxygen core viewed from above the central $[Mn^{III}_4Mn^{II}_2O_6]^{4+}$ ring; (d) an idealized icosahedron showing the positions of the Mn ions in **1** (pink) and the missing vertexes (blue); (e) binding mode of $thme^{3-}$.

Description of Structure. Labeled plots of **1** are given in Figure 1, and selected bond lengths and angles are given in Table 2. The metallic skeleton comprises a series of 10 edge-sharing triangles that describe part of an idealized icosahedron, in which 3 of the 12 vertexes are missing. The metal ions are centrally connected via a combination of seven oxides and three alkoxides. The $[Mn^{IV}_3Mn^{III}_4Mn^{II}_2O_7]^{14+}$ central core can be described as either a series of vertex- and edge-sharing $[Mn_3O]$ units or perhaps most easily as a $[Mn^{III}_4Mn^{II}_2O_6]^{4+}$ ring on which is sitting a smaller $[Mn^{IV}_3O]^{10+}$ ring. This $[Mn^{III}_4Mn^{II}_2O]^{4+}$ ring is trapped-valence with the Mn^{2+} ions being Mn4 and Mn8. The upper $[Mn_3O]^{10+}$ ring consists of only Mn^{4+} ions (Mn1−Mn3) and is capped on one side by the sole tripodal ligand, each arm of which (O1T−O3T) acts as a μ_2-bridge and on the other side by a μ_3-oxide (O1). The $[Mn^{IV}_3O]^{10+}$ unit is connected to the $[Mn^{III}_4Mn^{II}_2O]^{4+}$ ring via the six μ_3-oxides within the six-membered wheel and three carboxylates which bridge in their familiar syn, syn, μ-mode. The remaining carboxylates in the structure bridge between the Mn ions in the

(16) Perdew, J. P.; Burke, K.; Ernzerhof, M. *Phys. Rev. Lett.* **1996**, *77*, 3865−3868.
(17) van Vleck, J. *Phys. Rev.* **1937**, *52*, 1178−1198.
(18) (a) Pederson, M. R.; Khanna, S. N. *Phys. Rev. B* **1999**, *59*, 693−696R. (b) Pederson, M. R.; Khanna, S. N. *Phys. Rev. B* **1999**, *60*, 9566−9572.
(19) Kortus, J.; Pederson, M. R.; Baruah, T.; Bernstein, N.; Hellberg, C. S. *Polyhedron* **2003**, *22*, 1871−1876.

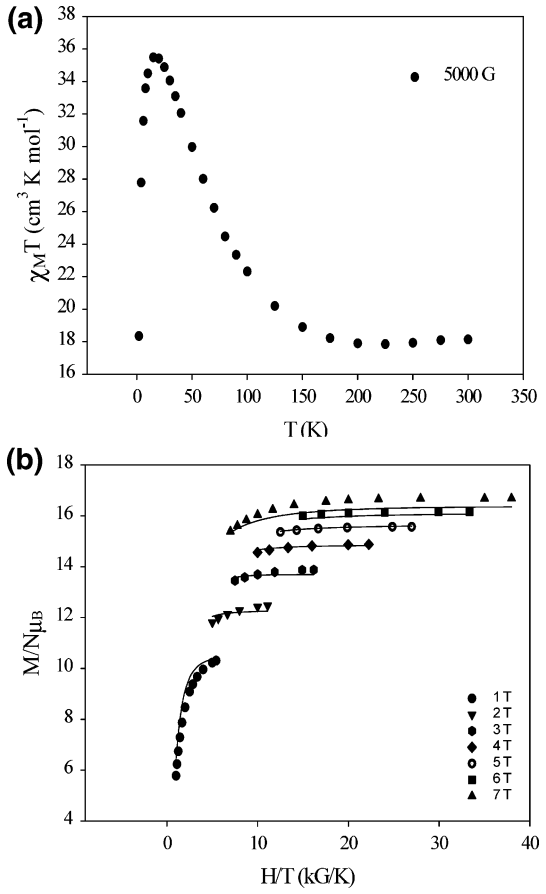

Figure 2. (a) Plot of $\chi_M T$ versus T for complex **1** measured in the temperature range of 1.8−300 K in a field of 5.0 kG. (b) Plot of reduced magnetization ($M/N\,\mu_B$) versus H/T for complex **1**. The solid lines are fits of the data to an $S = {}^{17}/_2$ state with $g = 1.97(3)$ and $D = -0.29$ cm^{-1}. Data were measured at 1−7 T and 1.8−4 K.

Table 1. Crystallographic Data for **1**

formula	$C_{52}H_{80}Mn_9N_6O_{35}$
M, g mol^{-1}	1843.68
crystal system	monoclinic
space group	$P2_1/n$
a, Å	13.745(3)
b, Å	23.688(5)
c, Å	23.259(5)
α, deg	90
β, deg	96.49(3)
γ, deg	90
V, Å^3	7524(3)
T, K	150(2)
Z	4
ρ_{calc} [g cm^{-3}]	1.628
crystal shape and color	brown blocks
crystal size [mm]	0.28 × 0.23 × 0.12
μ [mm^{-1}]	1.546
unique data	15403
unique data, ($I > 2\sigma(F)$)	13552
$R1$, $wR2$	0.0376/0.0939

$[Mn^{III}_4Mn^{II}_2O_6]^{4+}$ ring in the same manner. The remaining coordination sites are occupied by two water molecules and three pyridines. All of the Mn ions are in distorted octahedral geometries, with their oxidation states assigned using charge balance considerations, bond lengths, and bond valence sum (BVS) calculations (Table 3). The Jahn−Teller elongations of the Mn^{3+} ions all lie approximately perpendicular to the plane of the $[Mn^{III}_4Mn^{II}_2O_6]^{4+}$ ring.

In the crystal, the molecules of complex **1** pack in two directions, which are approximately perpendicular to each other, in a head-to-head and tail-to-tail fashion, meaning that there are two, approximately transverse, directions for the easy-axis of magnetization (vide infra).

Magnetochemistry. DC Magnetic Susceptibility. Variable temperature magnetic susceptibility data were collected on **1** in the temperature range of 300−1.8 K in an applied field of 5 kG (Figure 2). The room temperature $\chi_M T$ value of approximately 18 cm^3 K mol^{-1} remains constant until around 150 K, where it begins to increase to a maximum value of approximately 36 cm^3 K mol^{-1} at 20 K before dropping sharply below this temperature. The spin only ($g = 2$) value for a $[Mn^{IV}_3Mn^{III}_4Mn^{II}_2]$ unit is approximately 29 cm^3 K mol^{-1}. The maximum in $\chi_M T$ is indicative of a high-spin ground state, with the low temperature decrease assigned to zero-field splitting, Zeeman effects, and/or intermolecular antiferromagnetic interactions. To determine the spin ground state for complex **1** magnetization data were collected in the ranges of 10−70 kG and 1.8−4.0 K, and these are plotted as reduced magnetization ($M/N\mu_B$) versus H/T in Figure 2. For a complex entirely populating the ground state and experiencing no zero-field splitting, the observed isofield lines should superimpose and saturate at a value ($M/N\mu_B$) equal to gS. For **1**, this is clearly not the case and is suggestive of appreciable ZFS. The data were fitted by a matrix-diagonalization method to a model that assumes only the ground state is populated, includes axial zero-field splitting ($D\hat{S}_z^2$), and carries out a full powder average.[20] The corresponding Hamiltonian is given by

$$\hat{H} = D\hat{S}_z^{\,2} + g\mu_B\mu_0\hat{S}_z H_z \qquad (1)$$

where D is the axial anisotropy, μ_B is the Bohr magneton, μ_0 is the vacuum permeability, $\hat{S}_z$ is the easy-axis spin operator, and H_z is the applied field. The best fit gave $S = {}^{17}/_2$, $g = 1.97(3)$, and $D = -0.29$ cm^{-1}. The ground state can be rationalized by assuming an antiferromagnetic interaction between the ferromagnetically coupled Mn^{4+} ions in the $[Mn^{IV}_3O]^{10+}$ ring and the Mn^{3+} and Mn^{2+} ions in the $[Mn^{III}_4Mn^{II}_2O_6]^{4+}$ ring. This is analogous to the situation in $[Mn_{12}O_{12}(O_2CR)_{16}(H_2O)_x]^{n-}$ where the four ferromagnetically coupled Mn^{4+} ions couple antiferromagnetically with the surrounding eight Mn^{3+} ions resulting in a net spin of $S = 10$.[1b]

Ac Magnetic Susceptibility. Given the nature of S and the sign and amplitude of D for complex **1**, ac susceptibility studies were undertaken to see if **1** acts as a single-molecule magnet. When the rate at which the magnetization of a molecule relaxes is close to that of an applied ac field, an out-of-phase ac susceptibility signal (χ_M'') will be observed, in conjunction with a concomitant decrease in the in-phase susceptibility ($\chi_M'T$). At low temperature where thermal energy is not sufficient to overcome the barrier for relaxation, the magnetization of the molecule cannot keep in-phase with the oscillating field. At the temperature of the χ_M'' versus T maximum, the relaxation rate ($1/\tau$) equals the ac angular frequency ($\omega = 2\pi\upsilon$), and thus the measurement of peak maxima at several different frequencies provides $1/\tau$ versus T data (since $\omega = 1/\tau$) and the barrier to relaxation can then be estimated from the Arrhenius equation. Ac susceptibility studies were carried out in the 1.8−10.0 K

(20) *MAGNET*, Davidson, E. R.; Indiana University.

Table 2. Selected Bond Lengths (Å) and Angles (deg) for **1**

Mn(1)−O(2)	1.8139(18)	Mn(4)−O(7)	2.0992(18)	Mn(7)−O(5)	1.8605(18)
Mn(1)−O(3)	1.8595(18)	Mn(4)−O(2)	2.1193(18)	Mn(7)−O(4)	1.9111(18)
Mn(1)−O(1)	1.9046(17)	Mn(4)−O(29)	2.150(2)	Mn(7)−O(17)	1.9623(19)
Mn(1)−O(3T)	1.9197(18)	Mn(4)−O(14)	2.158(2)	Mn(7)−O(26)	1.983(2)
Mn(1)−O(11)	1.9309(18)	Mn(4)−O(1W)	2.217(3)	Mn(7)−O(2W)	2.197(2)
Mn(1)−O(1T)	1.9470(18)	Mn(4)−N(1A)	2.282(3)	Mn(7)−O(22)	2.219(2)
Mn(2)−O(5)	1.8146(18)	Mn(5)−O(2)	1.8565(18)	Mn(8)−O(5)	2.1142(18)
Mn(2)−O(4)	1.8700(18)	Mn(5)−O(3)	1.9077(18)	Mn(8)−O(6)	2.1159(19)
Mn(2)−O(1)	1.9014(17)	Mn(5)−O(24)	1.9489(19)	Mn(8)−O(18)	2.132(2)
Mn(2)−O(2T)	1.9278(18)	Mn(5)−O(15)	1.978(2)	Mn(8)−O(27)	2.169(2)
Mn(2)−O(12)	1.9300(18)	Mn(5)−O(111)	2.183(2)	Mn(8)−O(110)	2.221(2)
Mn(2)−O(1T)	1.9426(17)	Mn(5)−O(21)	2.224(2)	Mn(8)−N(1C)	2.281(3)
Mn(3)−O(6)	1.8024(18)	Mn(6)−O(3)	1.8822(19)	Mn(9)−O(6)	1.8755(18)
Mn(3)−O(7)	1.8069(18)	Mn(6)−O(4)	1.8840(18)	Mn(9)−O(7)	1.8779(18)
Mn(3)−O(1)	1.9255(18)	Mn(6)−O(16)	1.966(2)	Mn(9)−O(28)	1.9778(19)
Mn(3)−O(13)	1.9343(19)	Mn(6)−O(25)	1.9728(19)	Mn(9)−O(19)	1.9837(19)
Mn(3)−O(2T)	1.9883(18)	Mn(6)−O(211)	2.233(2)	Mn(9)−O(210)	2.197(2)
Mn(3)−O(3T)	1.9916(17)	Mn(6)−N(1B)	2.274(2)	Mn(9)−O(23)	2.237(2)
O(2)−Mn(1)−O(3)	84.48(8)	O(5)−Mn(2)−O(4)	83.77(8)	O(6)−Mn(3)−O(7)	84.89(8)
O(2)−Mn(1)−O(1)	94.97(8)	O(5)−Mn(2)−O(1)	95.52(8)	O(6)−Mn(3)−O(1)	96.03(8)
O(3)−Mn(1)−O(1)	92.22(8)	O(4)−Mn(2)−O(1)	93.35(8)	O(7)−Mn(3)−O(1)	94.93(8)
O(2)−Mn(1)−O(3T)	93.85(8)	O(5)−Mn(2)−O(2T)	94.88(8)	O(6)−Mn(3)−O(13)	95.00(8)
O(3)−Mn(1)−O(3T)	174.54(8)	O(4)−Mn(2)−O(2T)	175.11(8)	O(7)−Mn(3)−O(13)	94.18(8)
O(1)−Mn(1)−O(3T)	82.74(8)	O(1)−Mn(2)−O(2T)	82.08(7)	O(1)−Mn(3)−O(13)	166.26(8)
O(2)−Mn(1)−O(11)	94.25(8)	O(5)−Mn(2)−O(12)	94.06(8)	O(6)−Mn(3)−O(2T)	92.58(8)
O(3)−Mn(1)−O(11)	94.47(8)	O(4)−Mn(2)−O(12)	94.94(8)	O(7)−Mn(3)−O(2T)	174.02(8)
O(1)−Mn(1)−O(11)	169.09(8)	O(1)−Mn(2)−O(12)	167.94(8)	O(1)−Mn(3)−O(2T)	79.93(7)
O(3T)−Mn(1)−O(11)	90.84(8)	O(2T)−Mn(2)−O(12)	89.85(8)	O(13)−Mn(3)−O(2T)	91.43(8)
O(2)−Mn(1)−O(1T)	174.77(8)	O(5)−Mn(2)−O(1T)	174.49(8)	O(6)−Mn(3)−O(3T)	175.94(8)
O(3)−Mn(1)−O(1T)	90.76(8)	O(4)−Mn(2)−O(1T)	90.94(8)	O(7)−Mn(3)−O(3T)	93.55(8)
O(1)−Mn(1)−O(1T)	83.01(7)	O(1)−Mn(2)−O(1T)	83.21(7)	O(1)−Mn(3)−O(3T)	80.35(7)
O(3T)−Mn(1)−O(1T)	90.69(7)	O(2T)−Mn(2)−O(1T)	90.27(8)	O(13)−Mn(3)−O(3T)	88.85(8)
O(11)−Mn(1)−O(1T)	88.29(8)	O(12)−Mn(2)−O(1T)	87.91(7)	O(2T)−Mn(3)−O(3T)	88.61(7)
O(7)−Mn(4)−O(2)	93.84(7)	O(2)−Mn(5)−O(3)	81.99(8)	O(3)−Mn(6)−O(4)	96.47(8)
O(7)−Mn(4)−O(29)	85.72(8)	O(2)−Mn(5)−O(24)	95.17(8)	O(3)−Mn(6)−O(16)	174.07(8)
O(2)−Mn(4)−O(29)	179.43(8)	O(3)−Mn(5)−O(24)	173.96(9)	O(4)−Mn(6)−O(16)	88.89(8)
O(7)−Mn(4)−O(14)	176.70(8)	O(2)−Mn(5)−O(15)	173.90(8)	O(3)−Mn(6)−O(25)	89.48(8)
O(2)−Mn(4)−O(14)	83.23(8)	O(3)−Mn(5)−O(15)	93.32(8)	O(4)−Mn(6)−O(25)	173.57(8)
O(29)−Mn(4)−O(14)	97.22(8)	O(24)−Mn(5)−O(15)	89.12(8)	O(16)−Mn(6)−O(25)	85.06(8)
O(7)−Mn(4)−O(1W)	94.35(8)	O(2)−Mn(5)−O(111)	98.94(8)	O(3)−Mn(6)−O(211)	93.93(9)
O(2)−Mn(4)−O(1W)	94.23(8)	O(3)−Mn(5)−O(111)	96.54(8)	O(4)−Mn(6)−O(211)	98.14(8)
O(29)−Mn(4)−O(1W)	85.45(10)	O(24)−Mn(5)−O(111)	89.15(9)	O(16)−Mn(6)−O(211)	87.80(9)
O(14)−Mn(4)−O(1W)	87.41(10)	O(15)−Mn(5)−O(111)	85.43(9)	O(25)−Mn(6)−O(211)	83.83(8)
O(7)−Mn(4)−N(1A)	88.96(8)	O(2)−Mn(5)−O(21)	90.13(8)	O(3)−Mn(6)−N(1B)	90.31(8)
O(2)−Mn(4)−N(1A)	91.60(8)	O(3)−Mn(5)−O(21)	86.71(8)	O(4)−Mn(6)−N(1B)	91.54(8)
O(29)−Mn(4)−N(1A)	88.76(10)	O(24)−Mn(5)−O(21)	87.97(9)	O(16)−Mn(6)−N(1B)	86.99(9)
O(14)−Mn(4)−N(1A)	89.59(10)	O(15)−Mn(5)−O(21)	85.68(9)	O(25)−Mn(6)−N(1B)	85.98(8)
O(1W)−Mn(4)−N(1A)	173.09(10)	O(111)−Mn(5)−O(21)	170.69(8)	O(211)−Mn(6)−N(1B)	168.92(8)
O(5)−Mn(7)−O(4)	81.42(8)	O(5)−Mn(8)−O(6)	95.84(7)	O(6)−Mn(9)−O(7)	80.93(7)
O(5)−Mn(7)−O(17)	96.38(8)	O(5)−Mn(8)−O(18)	179.07(8)	O(6)−Mn(9)−O(28)	94.54(8)
O(4)−Mn(7)−O(17)	177.55(8)	O(6)−Mn(8)−O(18)	84.46(8)	O(7)−Mn(9)−O(28)	172.27(8)
O(5)−Mn(7)−O(26)	171.33(8)	O(5)−Mn(8)−O(27)	84.44(8)	O(6)−Mn(9)−O(19)	174.65(8)
O(4)−Mn(7)−O(26)	91.87(8)	O(6)−Mn(8)−O(27)	178.40(10)	O(7)−Mn(9)−O(19)	94.62(8)
O(17)−Mn(7)−O(26)	90.21(8)	O(18)−Mn(8)−O(27)	95.28(8)	O(28)−Mn(9)−O(19)	89.55(8)
O(5)−Mn(7)−O(2W)	97.34(8)	O(5)−Mn(8)−O(110)	93.51(8)	O(6)−Mn(9)−O(210)	97.68(8)
O(4)−Mn(7)−O(2W)	95.53(8)	O(6)−Mn(8)−O(110)	92.99(9)	O(7)−Mn(9)−O(210)	97.46(8)
O(17)−Mn(7)−O(2W)	85.82(8)	O(18)−Mn(8)−O(110)	87.34(9)	O(28)−Mn(9)−O(210)	89.32(9)
O(26)−Mn(7)−O(2W)	88.73(9)	O(27)−Mn(8)−O(110)	85.41(10)	O(19)−Mn(9)−O(210)	85.79(8)
O(5)−Mn(7)−O(22)	89.17(8)	O(5)−Mn(8)−N(1C)	87.34(8)	O(6)−Mn(9)−O(23)	89.36(8)
O(4)−Mn(7)−O(22)	89.99(8)	O(6)−Mn(8)−N(1C)	87.75(8)	O(7)−Mn(9)−O(23)	86.76(8)
O(17)−Mn(7)−O(22)	88.88(8)	O(18)−Mn(8)−N(1C)	91.80(10)	O(28)−Mn(9)−O(23)	86.93(9)
O(26)−Mn(7)−O(22)	85.32(9)	O(27)−Mn(8)−N(1C)	93.84(10)	O(19)−Mn(9)−O(23)	87.42(8)
O(2W)−Mn(7)−O(22)	172.01(8)	O(110)−Mn(8)−N(1C)	178.80(9)	O(210)−Mn(9)−O(23)	172.26(8)

range in a 3.5 G field oscillating at frequencies up to 1000 Hz. The in-phase ($\chi_M'T$) and out-of-phase (χ_M'') signals for **1** are shown in Figure 3. There is a frequency-dependent decrease in the $\chi_M'T$ signal and a frequency-dependent out-of-phase signal at $T \leq 4$ K. Both are strong indicators (but not definitive evidence) of SMM behavior. For complex **1**, the peak at 1000 Hz occurs at approximately 3.5 K. The data obtained were fit to the Arrhenius equation to give an effective energy barrier for the reorientation of the magnetization (U_{eff}) of 27 K, with $\tau_0 = 5.0 \times 10^{-8}$ s.

Single-Crystal Measurements. Hysteresis Studies. If complex **1** is an SMM, it should display hysteresis loops in magnetization versus field studies. Figure 4 shows just such a plot for **1**, at temperatures below 1.5 K and at a sweep rate of 0.001 T s^{-1} and at 1.05 K at sweep rates of 0.001−0.017 T s^{-1}, with the field applied in the direction of the easy-axis of half the molecules. For the other half, the field is approximately transverse. The hysteresis loops are sweep rate and temperature-dependent and are not smooth, showing steps at regular intervals of field indicative of quantum tunneling (QTM). The field separation between the zero-field resonance and the next for **1** is 0.27 T, giving $D/g = 0.129$ cm^{-1}. If we assume a value of $g = 2$, then the observed $D = -0.258$ cm^{-1} is in good agreement with that obtained from the bulk dc measurements.

Table 3. Bond Valence Sum (BVS) Calculations for the Metal Ions in **1**

	Mn^{II}	Mn^{III}	Mn^{IV}	assignment
Mn1	4.109	4.188	4.542	Mn^{IV}
Mn2	4.117	4.196	4.550	Mn^{IV}
Mn3	4.034	4.111	4.458	Mn^{IV}
Mn4	1.965	2.003	2.172	Mn^{II}
Mn5	3.140	3.200	3.471	Mn^{III}
Mn6	3.039	3.097	3.359	Mn^{III}
Mn7	3.090	3.149	3.415	Mn^{III}
Mn8	1.958	1.995	2.164	Mn^{II}
Mn9	3.082	3.141	3.407	Mn^{III}

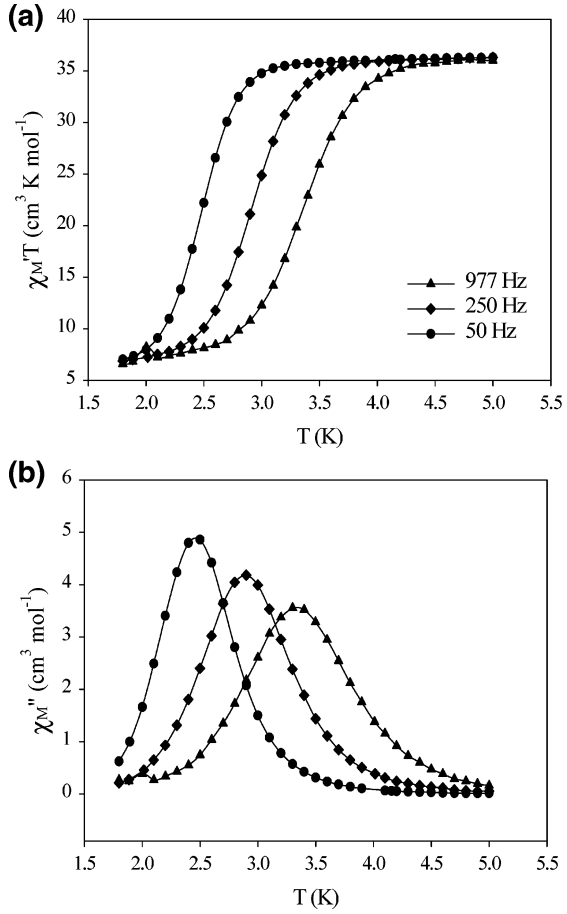

Figure 3. Plots of the in-phase (χ_M') signal as $\chi_M'T$ and out-of-phase (χ_M'') signal in ac susceptibility studies versus temperature in a 3.5 G field oscillating at the indicated frequencies.

Relaxation Studies using Ac and Dc Data. Relaxation data were also determined for **1** from dc relaxation decay measurements performed on single crystals using an array of micro-SQUIDS. First, a large dc field of 1.4 T was applied to each sample at 5 K to saturate the magnetization in one direction, and the temperature decreased to a specific value between 1.8 and 0.04 K. When the temperature was stable, the field was swept from 1.4 to 0 T at a rate of 0.14 T s^{-1} and the magnetization in zero-field measured as a function of time. A plot of the relaxation, plotted as a fraction of maximum value M_S, for complex **1** is shown in Figure 4. Combining this relaxation data with the ac data allows the construction of an Arrhenius plot of τ versus $1/T$. Above approximately 0.4 K the relaxation rate is temperature-dependent with the fits yielding $U_{eff} = 26.6$ K and $\tau_0 = 6.5 \times 10^{-8}$ s. Below 0.4 K, however, the relaxation rate is temperature-independent with a relaxation rate of 8×10^6 s. In this temperature regime, the relaxation of the magnetization occurs only via quantum tunneling as the thermally activated process becomes insignificant.

Inelastic Neutron Scattering (INS) Study of Undeuterated 1. Inelastic neutron scattering (INS) is a powerful tool to determine exchange couplings and single-ion anisotropies in molecular magnets.[21] Due to the spin of the neutron, there is a strong interaction between the magnetic moment of the neutron and the magnetic field created by the unpaired electrons in the sample. Measuring the INS intensity as a function of momentum and energy transfer provides useful information on the magnetic scattering function, $S(Q,\omega)$, which contains the details of the magnetic exchange interactions and anisotropy splittings.[22] Thus far, none of the above experimental studies has provided *direct* information on the nature and energies of energy splitting in the ground state of **1**. As a first approximation, one can use a giant spin model to describe the ground state, assuming that it is well isolated from the excited spin states. An effective Hamiltonian then describes the zero-field splitting of the giant spin ground state. The low symmetry of complex **1** allows for many higher order crystal field terms in the effective spin Hamiltonian. The fact that the Jahn−Teller axes of the four Mn^{III} ions all lie roughly perpendicular to the plane of the $[Mn^{III}_4Mn^{II}_2O_6]^{4+}$ ring and the presence of a pseudo 3-fold axis perpendicular to this ring justifies the use of an axial Hamiltonian in the first instance:

$$H_{axial} = D[\hat{S}_z^2 - S(S+1)/3] + B_4^0\hat{O}_4^0 \qquad (2)$$

where

$$\hat{O}_4^0 = 35\hat{S}_z^4 - [30S(S+1) - 25]\hat{S}_z^2 - 6S(S+1) + 3S^2(S+1)^2$$

The first term in eq 2 splits the ground state into $S + {}^1/_2$ Kramer's doublets, and for a negative D value, the $M_S = \pm S$ doublet lies lowest in energy. Equation 2, therefore, splits this ground state into nine $\pm M_S$ Kramer's doublets. The INS selection rule, $\Delta M_S = \pm 1$, predicts eight transitions for an $S = {}^{17}/_2$ ground state where the intensity for an $|M_S| \rightarrow |M_S + 1|$ INS transition can be calculated as

$$I(|M_S| \rightarrow |M_S+1|) \propto P(\pm M_S) \times \begin{pmatrix} S & 1 & S \\ -M_S & 1 & M_S+1 \end{pmatrix} \times \begin{pmatrix} S & 1 & S \\ -M_S-1 & 1 & M_S \end{pmatrix} \qquad (3)$$

where $P(\pm M_S)$ is the Boltzmann population of the initial state $\pm M_S$.

Figure 5 shows the INS spectra of **1** measured at 1.6 (10 h), 12 (31 h), and 20 K (25 h), summed over all scattering angles. Positive and negative energy transfer corresponds to neutron energy loss and gain, respectively. The 1.6 K spectrum exhibits one strong band at 3.72 cm^{-1} on the loss side with a second one coming up as a shoulder at lower energy. A series of hot bands is observed at 12 and 20 K. At this latter temperature, we measured the energy gain and the loss side. The peak energies are the same on both sides, and we can identify six

(21) Basler, R.; Boskovic, C.; Chaboussant, G.; Güdel, H.-U.; Murrie, M.; Ochsenbein, S. T.; Sieber, A. *ChemPhysChem* **2003**, *4*, 910−926.
(22) Böni, P.; Furrer, A.; Schefer, J. *Principles of Neutron Scattering*, Proceedings of the Eigth Summer School on Neutron Scattering, World Scientific Co. Pte. Ltd., 2000.

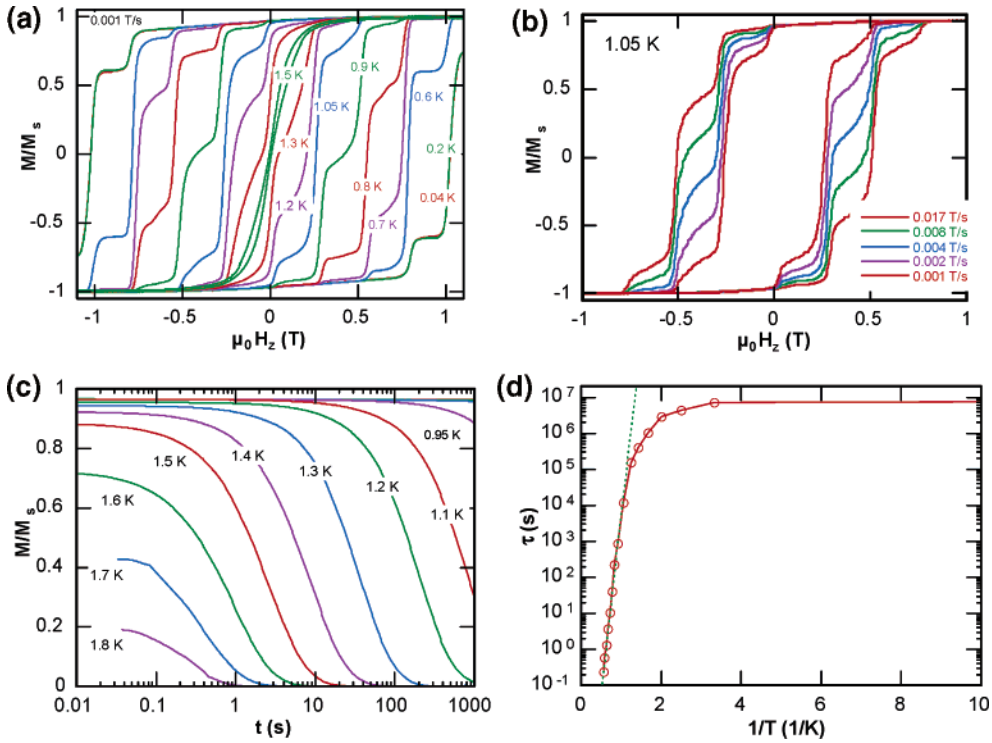

Figure 4. Magnetization (M) of **1** (plotted as fraction of maximum value M_S) versus applied magnetic field ($\mu_0 H$). The resulting hysteresis loops are shown at different temperatures (a) and different field sweep rates (b). Single-crystal relaxation data for **1**, plotted as fraction of maximum value M_S versus time (c). Arrhenius plot for **1** using ac data (χ_M'') and dc decay data on a single crystal. The solid line is the fit of the data in the thermally activated region, and the dashed line is the fit of the temperature-independent data.

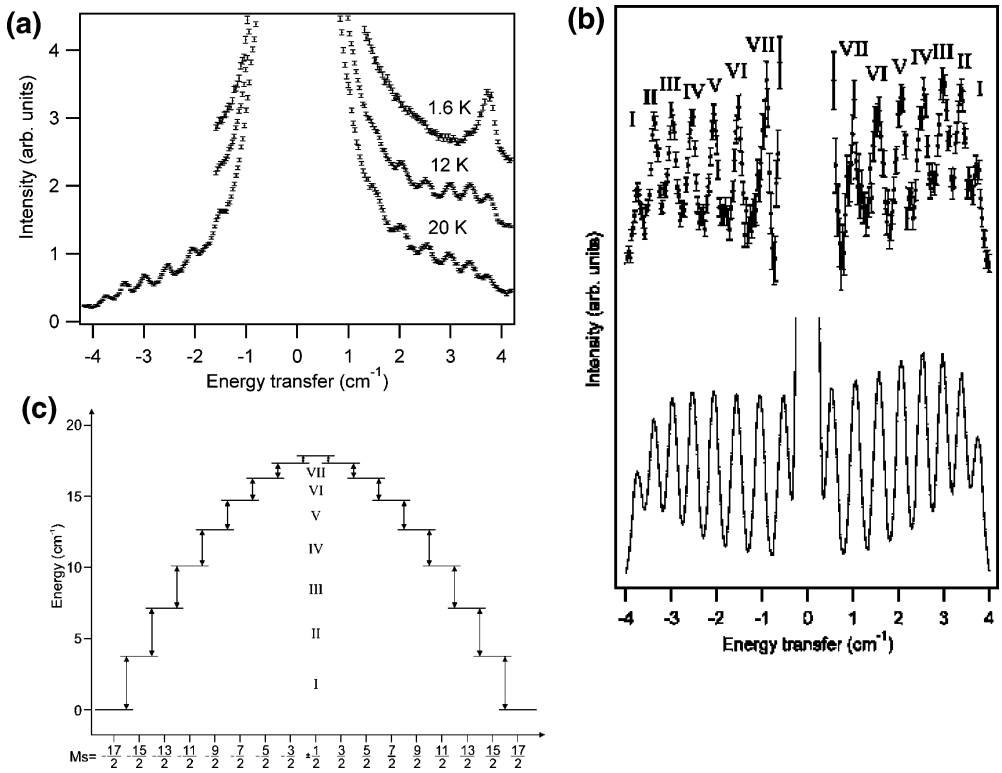

Figure 5. (a) INS spectra measured on IRIS with an analyzing energy of 1.84 meV at 1.6 (10 h), 12 (31 h) and 20 K (25 h), summed over all scattering angles. (b) INS spectrum of **1** measured at 20 K corrected for background (top) and calculated spectrum at 20 K using eqs 2 and 3 with the parameters $D = -0.249$ cm^{-1} and $B_4^0 = 7 \times 10^{-6}$ cm^{-1} (bottom). (c) Calculated anisotropy splitting of the $S = {}^{17}/_{2}$ ground state according to the Hamiltonian of eq 2 with parameter values of $D = -0.249$ cm^{-1} and $B_4^0 = 7 \times 10^{-6}$ cm^{-1}. The arrows correspond to the allowed $\Delta M_S = \pm 1$ INS transitions.

distinct maxima and a shoulder on the elastic line on either side of the spectrum. The peaks exhibit an almost regular picket fence pattern with decreasing peak separations toward higher energy transfer. On the basis of their temperature and Q-dependence, it is possible to assign the 14 observed bands to $\Delta M_S = \pm 1$ transitions within the ground state multiplet. The progression

of the peak positions is limiting the possible number of transitions in the ground state multiplet to exactly eight on either side.

Figure 5b shows the spectrum measured at 20 K after subtracting the nonmagnetic background. The peaks labeled I−VII correspond to the transitions shown in Figure 5c, which shows the energy splitting pattern of the $S = {}^{17}/_{2}$ ground state. Least-squares calculations using eq 2 and the peak positions determined by INS yield the following best parameter set ($D = -0.249(5)$ cm^{-1}, and $B_4^0 = 7(4) \times 10^{-6}$ cm^{-1}. The value of the axial anisotropy parameter, D, is in good agreement with the D values of -0.29 and -0.26 cm^{-1} derived from powder and single-crystal magnetic measurements, respectively. The use of a Hamiltonian without the fourth-order term, $B_4^0\hat{O}_4^0$, could not account for the observed decrease of the energy intervals with increasing energy transfer. The B_4^0 parameter must be positive, which is not without precedent in the spin cluster literature (positive B_4^0 values have been reported for the single-molecule magnets [Fe_8] and [Mn_4]).[23,24]

Figure 5 shows a calculated spectrum at 20 K using eqs 2 and 3 with the best fit parameters. The peak positions and relative intensities are in excellent agreement with the experimental data. For energy transfers below ± 1 cm^{-1}, the experimental data are dominated by the elastic line, and the eighth peak predicted by the calculations is not observable. The nonmagnetic scattering is orders of magnitude more intense than the magnetic scattering in the region of the elastic line, thus swamping the magnetic part. Physically, the strong central line with the pronounced tails in Figure 5a originates from elastic and quasi-elastic nonmagnetic scattering processes. Its intensity is enhanced by the presence of a large number of hydrogen atoms in the measured sample. At the low energy transfer of our experiment, it leads to an enhanced elastic line, including tails as well as a higher background. For a more accurate determination of peak VII in Figure 5b, it would be necessary to measure a deuterated sample. The incoherent nuclear scattering cross-section of deuterium is 40 times smaller than that of hydrogen; therefore, the effects described above are reduced drastically. Deuteration is often considered a prerequisite for a successful magnetic INS experiment, but the present study shows that data of remarkable quality can be obtained with an undeuterated sample in the energy transfer range between 1 and 4 cm^{-1}. The energy transfer region, in which magnetic cluster excitations can be observed despite the presence of hydrogen atoms, covers the range from about 1 to 30 cm^{-1}. We ascribe this to a low density of vibrational states with significant hydrogen contribution in this "lucky window".

Frequency Domain Magnetic Resonance Spectroscopy (FDMRS) of 1. FDMRS spectra were recorded on a polycrystalline powder pellet of complex **1** using linearly polarized radiation in the frequency range of 2.8−5.0 cm^{-1} and at temperatures between 1.8 and 30 K, in the absence of an external magnetic field. The spectra were normalized, that is, divided by the 30 K spectrum to remove the oscillation of the baseline caused by Fabry−Perot-like interference within the plane parallel sample as well as artifacts caused by standing waves.

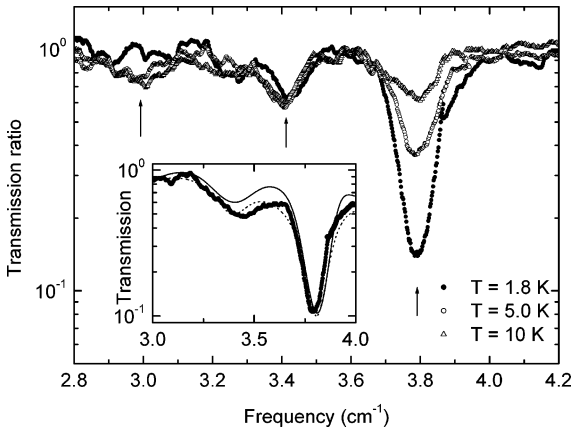

Figure 6. Normalized FDMRS spectra recorded on a pressed powder pellet of **1** at various temperatures, as indicated in the figure. The inset shows the 1.8 K non-normalized spectrum together with fits assuming Gaussian (solid line) and Lorentzian (dotted line) line shape functions.

In the normalized spectra (Figure 6), three resonance lines can be observed at $\nu = 3.79$, 3.41, and 2.95 cm^{-1}. The exact positions of the resonance lines were determined by fitting them with high degree polynomials. The obtained resonance frequencies were then used in the fitting procedure. From the fact that the highest frequency resonance line has highest intensity at the lowest temperatures, it can immediately be concluded that the D term in the zero-field splitting Hamiltonian must be negative. A first value of this parameter was determined by searching the minimum discrepancy between calculated and observed resonance frequencies. Introducing an E term and minimizing the discrepancy factor in two dimensions leads to a value that is practically zero and did not significantly decrease the discrepancy factor. A significantly better fit is obtained when a B_4^0 term is included. Adding transverse anisotropy in fourth order (a B_4^3 term in the case of trigonal symmetry) also did not improve the fit. Finally, the best fit parameters were determined to be $D = -0.247 \pm 0.005$ cm^{-1} and $B_4^0 = (+4.6 \pm 0.1) \times 10^{-6}$ cm^{-1}. This means that the system is completely axial and that the M_S states are the eigenstates of the system. The observed resonance lines correspond, therefore, to the transitions $|M_S = \pm 17/2> \rightarrow |M_S = \pm 15/2>$ (3.79 cm^{-1}), $|M_S = \pm 15/2> \rightarrow |M_S = \pm 13/2>$ (3.41 cm^{-1}), and $|M_S = \pm 13/2> \rightarrow |M_S = \pm 11/2>$ (2.95 cm^{-1}).

From the obtained spin Hamiltonian parameters, the spectra can be simulated. To this end, the magnetic permeability of the sample calculated from the sum of the contributions due to the various resonance modes and the dielectric permeability obtained from the oscillations of the baseline and the thickness of the sample were used. The transmission spectrum is calculated from them using Fresnel's formulas.[25] The inset in Figure 6 shows that the spectrum can be very well simulated. The simulation assuming a Gaussian line shape is slightly better than that assuming a Lorentzian one, but definitive conclusions are difficult to draw. Indeed, if line broadening contributions due to both homogeneous and inhomogeneous processes are of the same order, the line shape might be intermediate between these two extremes.

Theoretical Studies: DFT Calculations. Using the structural model described in the Experimental Section, we carried out

(23) Caciuffo, R.; Amoretti, G.; Murani, A.; Sessoli, R.; Caneschi, A.; Gatteschi, D. *Phys. Rev. Lett.* **1998**, *81*, 4744−4747.
(24) Yoo, J.; Yamaguchi, A.; Nakano, M.; Krzystek, J.; Streib, W. E.; Brunel, L.-C.; Ishimoto, H.; Christou, G.; Hendrickson, D. N. *Inorg. Chem.* **2001**, *40*, 4604−4616.
(25) Dressel, M.; Grüner, G. *Electrodynamics of Solids*; Cambridge University Press: Cambridge, U.K., 2002.

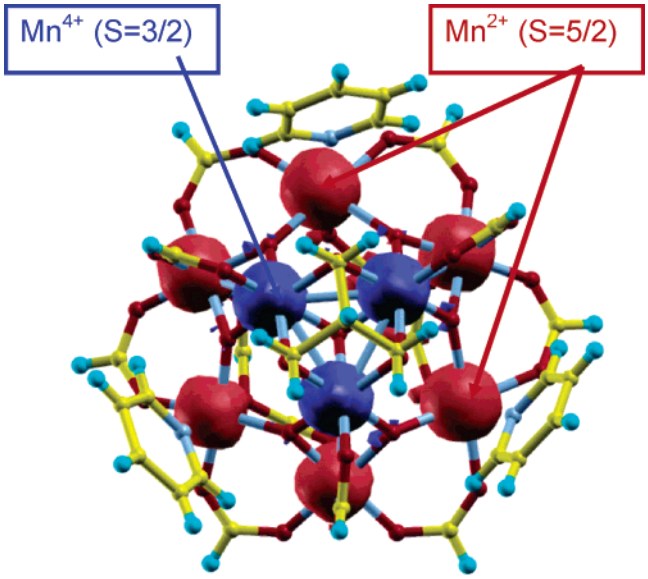

Figure 7. Plot of the spin density obtained from first-principles DFT calculations. Red corresponds to "spin up" and blue to "spin down".

DFT calculations at the all-electron level on a single-molecular entity. During the self-consistent cycle, we did not apply any constraint on the total moment of the cluster, allowing a search of the full space of magnetic moments. The calculation converged to a ground state with 17 unpaired electrons, in agreement with the experimental findings. The magnetic ordering is shown in Figure 7 by a plot of the spin density.

To identify the charge state of the Mn ions, we calculated the magnetic moment within a sphere of radius 1.2 Å centered at the Mn site. For the three inner Mn(IV) ions with "spin down" electrons, we obtained a magnetic moment of $-2.4\ \mu_B$. The outer ring of Mn ions all have "spin up" electrons with two Mn ions displaying $4.3\ \mu_B$ and the remaining Mn ions having values of 3.3, 3.5 ($\times 2$), and $3.6\ \mu_B$. Considering that this method of calculating the magnetic moment will not include all contributions to the spin density of a given atom, one can conclude that the closest ionic picture is fully consistent with the earlier experimental findings of two Mn(II) and four Mn(III) ions being spin up and three Mn(IV) ions being spin down, resulting in the $S = {}^{17}/_{2}$ spin ground state of the molecule.

Using self-consistent wave functions[18,19] allows us to take into account all second-order contributions to the magnetic anisotropy due to spin−orbit interactions. These contributions can be expressed in the form of a simple spin Hamiltonian with only quadratic terms in the spin operators:

$$H = DS_z^2 + E\,(S_x^2 - S_y^2) \qquad (6)$$

The rhombohedral anisotropy parameter, E, vanishes for uniaxial systems due to symmetry, but for lower symmetry systems, such as the one considered here, it may have a nonzero value. The final results obtained from the NRLMOL first-principles DFT calculation are $D = -0.23\ \text{cm}^{-1}$ and $E = 0.035\ \text{cm}^{-1}$. Therefore, the system is an easy-axis system with a magnetic anisotropy barrier of 26.2 K. The value of the axial D is in very good agreement with the experimental observation and of similarly good quantitative agreement with values found for other single-molecule magnets.[19]

Table 4. Comparison of zfs Parameters Obtained by FDMRS, INS, Reduced Magnetization versus *H*/*T* Measurements, and Single-Crystal Measurements on **1**

zfs (cm^{-1})	FDMRS	INS	magnetization	μ-SQUID	DFT
D	-0.247 ± 0.005	$-0.249(5)$	$-0.29(3)$	-0.258	-0.235
B_4^0	$(+4.6 \pm 0.1) \times 10^{-6}$	$+7(4) \times 10^{-6}$			

We would like to stress here that there is no experimental input besides the molecular structure and no free adjustable parameter. The numerical accuracy of the calculated value of D with respect to the basis set and other purely numerical parameters is estimated to be of the order of 0.01 cm^{-1}, and similar changes are expected for small changes in the geometry of the cluster. However, this error estimate does not include systematic deviations due to the approximate nature of DFT, which may result in a D value smaller by a factor of 2 compared with that of experiment.[26] The coupling of the vibrational degrees of freedom to the spin may give rise to fourth-order contributions to the magnetic anisotropy energy. While in principle it is possible to calculate these contributions,[27] we have not attempted this because it was computationally too expensive with our currently available resources. However, considering the small value of the fourth-order contribution indicated from experiment, our numerical accuracy may not be sufficient for such an estimate.

Conclusions

Reaction of $[Mn_3O(O_2CMe)_6(py)_3]$ with the tripodal ligand H_3thme (1,1,1-tris(hydroxymethyl)ethane) produces the complex $[Mn_9O_7(O_2CCH_3)_{11}(thme)(py)_3(H_2O)_2]$ whose mixed-valent metallic skeleton describes part of an idealized icosahedron. Magnetic studies using a variety of techniques, including bulk and single-crystal magnetometry, inelastic neutron scattering, frequency domain magnetic resonance spectroscopy, and theoretical density functional calculations, show the complex to possess a spin ground state of $S = {}^{17}/_{2}$. The ground state arises from the antiferromagnetic coupling between the central Mn^{4+} ions and the peripheral Mn^{3+} and Mn^{2+} ions. Hysteresis loops at ultralow temperatures show the complex to be a single-molecule magnet with an energy barrier of approximately 27 K.

Acknowledgment. We wish to thank Grégory Chaboussant, Felix Fernandez-Alonso, and Stefan T. Ochsenbein for assistance in the collection of INS data. We also thank Lloyd's of London Tercentenary Foundation and the EPSRC (UK) for funding.

Supporting Information Available: Cartesian coordinates used for the DFT calculation, and complete refs 5, 8d, and 13. This material is available free of charge via the Internet at http://pubs.acs.org.

JA042302X

(26) Cirera, J.; Kortus, J.; Ruiz, E. To be published.
(27) Pederson, M. R.; Bernstein, N.; Kortus, J. *Phys. Rev. Lett.* **2002**, *89*, 097202−1/4.